PCCP

PAPER

View Article Online
View Journal | View Issue

Cite this: *Phys. Chem. Chem. Phys.*, 2016, **18**, 1451

The impact of doping rates on the morphologies of silver and gold nanowires grown in helium nanodroplets

Alexander Volk,[a] Philipp Thaler,[a] Daniel Knez,[b] Andreas W. Hauser,*[a] Johannes Steurer,[a] Werner Grogger,[b] Ferdinand Hofer[b] and Wolfgang E. Ernst*[a]

Received 15th October 2015,
Accepted 12th November 2015

DOI: 10.1039/c5cp06248a

www.rsc.org/pccp

Silver and gold nanowires are grown within superfluid helium nanodroplets and investigated by high resolution electron microscopy after surface deposition. The wire morphologies depend on the rate of metal atom doping in the pickup sequence. While high doping rates result in a polycrystalline face-centered cubic nanowire structure, at lower doping rates the initial fivefold-symmetry seems to be preserved. An explanation for this observation is given by computer simulations, which allow the derivation of timescales for the nanowire growth process inside helium nanodroplets.

1 Introduction

Quantized vortices, accessory phenomena of superfluidity, were predicted by Onsager and Feynman around 1950.[1,2] Despite earlier experimental evidence for their existence,[3,4] it took until 2006 to finally image them in bulk superfluid helium (He II) using hydrogen particles as tracers.[5] The fact that impurities get pinned to the vortices as a consequence of a pressure gradient around the vortex cores[6] can be exploited to investigate processes such as vortex reconnection and quantum turbulence in He II.[7–9] In a more applied approach, the use of the directed growth of nanoparticles in the presence of vortices in He II was proposed for the production of nanowires.[10] Single and bundled metal nanowires were obtained from laser ablation of metal targets immersed in He II and subsequently characterized in terms of structure, electrical properties and thermal stability.[11–20]

Helium nanodroplets (He_N), on the other hand, were extensively used as weakly perturbing cryogenic matrices for the spectroscopy of atoms, molecules and small clusters in molecular beam experiments (see ref. 21–24 for detailed reviews). The possibility of sequential doping and local confinement of different species at 0.37 K makes He_N also a unique environment for cluster growth.[21–23,25,26] The first surface deposition of He_N-grown metal clusters[27,28] triggered a series of experimental studies on cluster growth and follow-up surface deposition.[29–33] Gomez *et al.* found that Ag nanoparticles (Ag_n), synthesized in single helium droplets and subsequently deposited on a substrate, tend to agglomerate equidistantly along distinct lines.[34] In the absence of external guiding forces, this can be taken as the first experimental evidence for the existence of vortices inside of He_N. This confirms several preceding computational studies on this issue (see ref. 35–38 and references therein). Further proof for the presence of vortices or even vortex lattices in the droplets was given by recent X-ray diffraction experiments on a Xe-doped He_N-beam and complementary density functional theory (DFT) calculations.[39,40] Utilizing these vortices as inert templates, continuous monometallic nanowires with lengths of several hundred nanometers were synthesized inside He_N,[41] as well as bimetallic core–shell nanowires.[42] As an intrinsic property of the growth process, the diameter of these wires is $\approx$3–10 nm. In a recent study on the stability of He_N-grown Ag nanowires we could show that these thin structures segment due to thermally induced Ag atom diffusion after their deposition on a surface.[43]

Despite these experimental achievements, little is known about the actual growth process of nanowires inside the droplets.[41,44] Our group was able to deduce a possible growth mechanism for pure Ag_n inside of vortex-free He_N by analyzing high resolution transmission electron microscopy (HRTEM) images of the deposited clusters.[30] A computational survey of the landing process revealed that small Ag_n (diameter $d_{Ag} < 3$ nm) presumably undergo reconstruction upon deposition, while for larger clusters the pronounced soft landing conditions[28,45,46] favour the conservation of the initial morphology.[47] Only recently we modelled the collision process between two coinage metal dopants in small He_N with a molecular dynamics (MD)

[a] *Institute of Experimental Physics, Graz University of Technology, Petersgasse 16, A-8010 Graz, Austria. E-mail: andreas.w.hauser@gmail.com, wolfgang.ernst@tugraz.at; Fax: +43 (316) 873 108140; Tel: +43 (316) 873 8157, +43 (316) 873 8140*

[b] *Institute for Electron Microscopy and Nanoanalysis & Graz Centre for Electron Microscopy, Graz University of Technology, Steyrergasse 17, A-8010 Graz, Austria*

simulation.[48] The obtained timescales for dimer collisions were subsequently used in a model suitable for larger droplet sizes. It shows that for large He_N, multicenter aggregation leads to well separated clusters in one droplet for long timescales.[49]

In the present study we extend our previous work by investigating the influence of the doping conditions on the cluster growth and aggregation inside of large He_N. We further give timescales for the pinning of clusters due to attractive forces exerted by vortices present in the droplets, which causes the nanowire-growth. The obtained results are compared to HRTEM images of bare Ag and Au clusters and nanowires. Experiment and calculations indicate that an alteration in the amount of metal dopants induces different growth scenarios, which finally influences the morphology of the produced nanowires. To our belief a good understanding of the underlying growth process of nanowires in He_N is one of the key questions to be addressed in order to be able to synthesize more elaborate structures with this technique.

2 Experimental

The experimental setup is described in detail elsewhere.[50] In brief, He_N are produced by the supersonic jet expansion of gaseous He (99.9999% purity) through a precooled nozzle with a 5 μm orifice into high vacuum. The helium stagnation pressure (p_0) was kept at 20 bar for all experiments discussed in this work. By variation of the nozzle temperature (T_0) it is possible to alter the mean droplet size ($\bar{N}$).[21] In our experiments, vortices have exclusively been observed for $T_0 \leq 6.5$ K at $p_0 = 20$ bar. Therefore, it can be assumed that they are efficiently created and preserved only when large He_N ($\bar{N} > 10^8$ atoms) are formed *via* breakup of liquid He during the expansion process.[34,51,52] For experiments on vortex-free He_N we therefore keep T_0 at 8 K. In all other cases, T_0 is set to 5.4 K. This corresponds to $\bar{N} \approx 7 \times 10^6$ atoms (droplet diameter $\bar{d}_D \approx 85$ nm) and $\bar{N} \approx 1.7 \times 10^{10}$ atoms ($\bar{d}_D \approx 1100$ nm) respectively.[21,51,53] We note that recent calculations also suggest vortex nucleation in small He_N ($N = 1000$) by ionization of attached dopants[54,55] or during the doping process with neutral atoms.[56] However, in the latter case theory suggests limited vortex-lifetimes in the picosecond range.

The He_N-beam passes a 400 μm skimmer into a separate vacuum chamber where the droplets are doped with the desired metal. Ag or Au atoms are evaporated from separate resistively heated alumina ovens of 2.3 cm length. They are captured by the passing droplets, in which they subsequently agglomerate to clusters. After the pickup, the droplet beam enters a UHV chamber (base pressure $<6 \approx 10^{-10}$ mbar) and is terminated on commercial TEM grids (Ted Pella, Inc., Prod. No. 01824). This leads to the disintegration of the droplet and a soft deposition of the contained aggregates on the amorphous carbon (a-c) surface.[28,45–47]

The disintegration of the He_N causes a rise in the He background pressure p_{He}, which can be monitored with an ionization pressure gauge (Leybold Heraeus IM 220) and a quadrupole residual gas analyzer (Balzers QMA 200/QME 200), both mounted off the beam axis. Due to evaporative cooling,[53] the He_N size and accordingly the total He flux Φ_{He} into the last chamber are reduced with increasing Ag/Au doping rate. Following ref. 28, we calculate the mean number of metal dopant atoms $\bar{n}_X$ per He_N as

$$\bar{n}_X = \frac{\left(\Phi_{He,undoped} - \Phi_{He,doped}\right) \times \bar{N}}{\Phi_{He,undoped}} \times \frac{E_{He}}{E_X} = \alpha \times \frac{\bar{N} \times E_{He}}{E_X}, \quad (1)$$

where the index X denotes either Ag or Au. The attenuation of the He_N beam due to doping is denoted as α and $E_{He} = 0.6$ meV is the binding energy of 1 He atom to the droplet.[53] $E_{Ag} = 3$ eV and $E_{Au} = 3.8$ eV are the bulk binding energies for Ag and Au, respectively.[57] This approach neglects the kinetic energy transfer to the droplet by the dopant atoms, which is two orders of magnitude smaller than the binding energy. Table 1 contains the values for $\bar{n}_X$ as obtained for the attenuations used in this work. We note that E_X is dependent on the cluster size and considerably smaller at the beginning of cluster growth.[58] This is taken into account for the small He_N ($\bar{N} \approx 7 \times 10^6$) in Table 1.

Table 1 Number of dopant atoms $\bar{n}_X$ per He_N for different droplet sizes $\bar{N}$ and attenuations α as calculated with eqn (1)

α	$\bar{N}$	n_{Ag}	n_{Au}
0.75	1.7×10^{10}	2.6×10^6	2.0×10^6
0.5	7×10^6	—	650
0.2	1.7×10^{10}	6.8×10^5	5.4×10^5
0.04	1.7×10^{10}	—	1.1×10^5

For the given average droplet speed $v_D \approx 173$ m s^{-1} at $T_0 = 5.4$ K[51] the pickup rates reach up to 2×10^{10} atoms per s. The energy transferred to the droplet this way leads to an estimated increase of the droplet temperature from 0.37 K[59] to ≈1.05 K.[53,60] Since this temperature is still below the He superfluid transition temperature of 2.17 K, quantized vortices are preserved during the pickup.

As for a previous study,[30] we use a Tecnai TF20 from FEI Company for TEM and HRTEM measurements on the deposited clusters and nanowires. The microscope is equipped with an FEG source and a high resolution Gatan imaging filter with an UltraScan CCD camera (2048 px × 2048 px). All images are recorded with 200 kV acceleration voltage and a current density as low as 1 pA nm^{-2} to prevent morphology changes of the particles during the imaging process.

Since the breakup of Ag nanowires becomes noticeable already at ≈260 K,[43] some substrates are cooled *via* the substrate holder to liquid nitrogen (LN_2) temperature for the investigation of continuous wires. After nanowire deposition, cooled substrates are immersed into LN_2 within 5 s after the substrate holder has been detached from its mount in the chamber. These substrates are subsequently transferred to a suited cryo-TEM holder (Gatan, Model 792) without being removed from the LN_2 bath. Other substrates are exposed to ambient conditions for times shorter than 5 min when transferred to the TEM. In all cases, the chamber is vented with gaseous N_2 (grade 5).

3 Computational details

3.1 Cluster growth and aggregation

Recently, we investigated the time dependence of two-particle-collisions in He_N *via* a combination of helium density functional theory and molecular dynamics simulations.[48] While it is computationally feasible to simulate the collision of just two dopants within a droplet on quantum-chemistry level, a similar description of the actual particle growth process is not possible due to the large time-scale (milliseconds) and the system size (up to 10^6 metal atoms). Instead, we use the collision times calculated in ref. 48 as input for a simplified, global model of multiple cluster growth in large helium droplets. We study the number and mass of all metal particles as a function of time without keeping track of actual particle positions. Qualitatively, the model is the same for simulations of Au and Ag dopants. Therefore, only the Ag case shall be described here in greater detail.

According to the real experiment, cluster growth in He_N starts by the pickup of single atoms in a locally defined region. In the computer simulation we therefore add $\bar{n}_{Ag}$ (see Table 1) atoms with a fixed doping frequency. The latter is determined by the length of the pickup region and the velocity of the droplets in the He_N beam. Benchmark calculations show that the shrinking of the droplet due to evaporative cooling has a negligible impact on the doping cross-section for a fixed dopant vapor pressure. Therefore a constant doping frequency can be assumed. The dopants are spawned within the He_N volume at Landau velocity $v_\lambda \approx 56$ m s^{-1}.[61] The time it takes for two atoms to aggregate $\Delta t_a(2)$ is taken from ref. 48 and adjusted as follows: as more dopant-atoms are added to the droplet, the nucleation rate will increase until equilibrium conditions are reached. In our model, the nucleation frequency $\left(\frac{1}{\Delta t_a(j)}\right)$ increases with the number of pairs that can be formed by j particles, hence

$$\Delta t_a(j) = \frac{2 \times \Delta t_a(2)}{j^2 - j}. \quad (2)$$

The shrinking of He_N due to evaporative cooling leads to a decrease of $\Delta t_a(2)$ according to ref. 48, which is considered in the simulation. On the other hand, assuming inelastic collisions and conservation of momentum, the velocity of metal clusters consisting of n atoms must decrease with increasing n ($n > 1$),

$$v(n) = v_\lambda \times \sqrt{\frac{8}{3\pi n}} \quad (3)$$

causing a growth of $\Delta t_a(2)$ proportional to $\frac{v_\lambda}{v(n)}$.

An individual "aggregation timer" is defined for every particle enclosed in the droplet, which reflects the actual droplet size and its current loading with dopants, *i.e.* the size-dependent velocities of all clusters which are currently present in the droplet. For the first two atoms picked up by the droplet this timer is set to $\Delta t_a(2)$, but it is reevaluated after every additional pickup following eqn (2) and (3). Whenever an aggregation timer expires, the corresponding particle merges with another particle randomly chosen from the current set, but with a probability proportional to the velocity of the second particle (*i.e.* mergers with smaller particles are preferred). The merging leads to the growth of the first particle and to a reevaluation of its aggregation timer according to eqn (3), while the second particle is removed from the set.

In order to study structural changes in our set of metal particles over time, we further keep track of the shape of each resulting particle, which is determined by the amount of binding energy released during coalescence. While the addition of single atoms to a preexisting cluster is treated in a way that yields a new spherical particle, two clusters only coalesce into a spherical particle if the released energy is large enough to completely melt at least one of the involved clusters. This treatment is based on the findings in ref. 14 and 16. The authors of the respective studies showed that the surface energy released upon coagulation of two small metal clusters in He II can lead to melting and a subsequent merging of the individual particles into a single sphere. For larger clusters the released energy may not be sufficient for a complete melting, so that the clusters stick together and form nanowires.

We use a slightly different approach to calculate the energy released upon coagulation, as this allows us a better implementation of coagulation events between different sized clusters. To start, we calculate the binding energy per atom $E_b(n)$ in a cluster consisting of n atoms using the empirical relation[62]

$$E_b(n) = E_{Ag} + 2^{\frac{1}{3}}\left(\frac{1}{2}D_e - E_{Ag}\right)n^{-\frac{1}{3}} \quad (4)$$

to estimate the released binding energy during the coalescence of two clusters consisting of n_1 and n_2 atoms respectively, as

$$\Delta E_b = (n_1 + n_2) \times E_b(n_1 + n_2) - (n_1 \times E_b(n_1) + n_2 \times E_b(n_2)). \quad (5)$$

$E_{Ag} \approx 3$ eV[57] denotes the Ag bulk binding energy and $D_e = 1.65$ eV[58] the binding energy of the Ag dimer. Both collision partners receive half of the released energy ΔE_b and the accompanying increase of the temperature of the clusters is evaluated by the simple approximation of the Dulong–Petit law. Clusters are considered as melted if their temperature exceeds the bulk melting temperature. Melting point depressions and latent heat are counteracting effects which are neglected due to their computationally difficult implementation for the given case of a time-dependent, broad cluster size distribution. Clusters which do not melt during coalescence are treated as one elongated particle. The particle size gets extended in only one dimension upon collision in order to simulate the process of nanowire formation. The new diameter is calculated as the mean diameter of the individual building blocks. The total number of individual particles (atoms, clusters and nanowires) contained in a single droplet (j) and the number of atoms (n_{sp}) within each spherical metal cluster (partially coalesced to wires) are tracked in the course of the computations. In the simulations, the clusters are cooled by their helium environment at a

constant cooling rate r_c which depends on the particle surface area. This rate is adjusted to reflect the experimental results, meaning that the mean cluster diameters obtained from n_{sp} at the end of the simulation time should be comparable to the nanowire diameters observed in the experiment. We find that $r_c \approx 190\ \mathrm{W\,cm^{-2}}$ reflects the experimental findings best. A change in r_c of +20% decreases the mean cluster diameters obtained at the end of the growth process by $\approx$25%, while a decrease in r_c of 20% increases the observed diameters by up to 50%. Gordon *et al.* derived the maximum diameter for which two equally sized metal spheres coagulate into a final spherical particle inside of He II, for several different metals by considering the release in surface energy during coalescence.[14] The values for r_c used in this work are considerably higher than those assumed in ref. 14, but still lower than the maximum cooling rates observed for small molecules in other He_N experiments.[63,64]

It is evident that without additional effects, given sufficient time, such an algorithm inevitably leads to one single final particle. In the real experiment the growth rates are damped due to the presence of vortices in large He_N. Particles caught by vortices are pinned to the vortex core and their motion is subsequently restricted to the direction along the vortex line.[5,65] The coalescence of captured particles along the vortex core is the reason for the formation of continuous nanowires, but is not directly captured in the presented model. However, we can choose the maximum simulation time to be equal to the mean time it takes for a particle to get trapped by a vortex contained in the He_N, which will be derived in the next section. This enables us to follow the growth of the building blocks of the final nanowires.

3.2 Cluster capture by vortices

Due to a pressure gradient around the vortex core,[6] a vortex exhibits an attractive force on particles in the droplet, whose magnitude is given by[66–68]

$$F_{far} \approx \left(\frac{a}{s}\right)^3 \frac{\rho_s \kappa^2}{3\pi} \tag{6}$$

for spherical particles in the far field and by

$$F_{near} \approx \rho_s \kappa^2 \log\left(\frac{a}{\zeta}\right) \tag{7}$$

near the vortex core, with a the radius of the particle, s the particle's normal distance to the vortex center, ζ the vortex core diameter, ρ_s the density of He II and $\kappa = h/m_{He}$ the quantum of circulation with h the Planck constant and m_{He} the atomic mass of He. In the simplest case where only one vortex is spanned across the droplet along the z-axis, $\bar{s}$ can be given analytically as

$$\bar{s} = \frac{3\pi}{16}\frac{d_D}{2} \tag{8}$$

We assume only one vortex per droplet for the following calculations. This assumption does not affect any of our arguments substantially. As estimated in the experimental section, the maximum He_N temperature does not exceed 1.05 K, resulting in a maximum fraction of normal fluid in the superfluid droplets of $\approx$1%.[6] After the pickup process, the droplet temperature will rapidly decrease to 0.37 K, so that the non-superfluid part will become negligibly small. Together with the low velocities of clusters within the droplets, this justifies the neglect of the Stokes drag on the particles. The acceleration of particles towards the vortex due to the attractive forces given above can then be calculated simply by the application of Newton's equation of motion. The far-field and near-field forces of eqn (6) and (7) are continuously connected to a resulting attractive force, and the equation of motion is numerically solved for the time t_{trap} it takes to get a particle trapped by a vortex core. We note that t_{trap} is nearly unaffected by an alteration of the particle radius a, since the corresponding increase of F_{far} is compensated by an equivalent increase of the particle's mass, while the influence of the short ranging F_{near} on t_{trap} is negligible. t_{trap} is chosen as the maximum simulation time for the cluster aggregation process, as for later times a significant amount of particles is restricted in the direction of motion.

4 Results and discussion

4.1 HRTEM images

In order to ensure that the fundamental growth process for different coinage metal clusters in vortex-free He_N ($\bar{N} \approx 7 \times 10^6$ atoms) is the same, we repeat our previous experiment,[30] but dope the droplets with Au instead of Ag. The TEM substrate is exposed to the Au-doped (α = 0.5) He_N-beam for 480 s. Following the routine of ref. 30, the mean diameter of deposited Au_n is measured using the image processing package FIJI.[69] The obtained diameter $\bar{d}_{Au} \approx 2.9(1)$ nm corresponds to $\bar{n}_{Au} \approx 750$ assuming a spherical cluster shape and bulk density of the metal.[30] The discrepancy between this value and the one given in Table 1 lies within the measurement uncertainties. We note that even small deviations in either of the variables in eqn (1) lead to a reasonable change in the estimated absolute number of dopants. Fortunately, this becomes less crucial for the larger droplets investigated.

HRTEM images are recorded and compared to the corresponding simulations[30,70] in order to determine the morphologies of the clusters. While a complete analysis of the Au_n morphology distribution lies beyond the scope of this article, we report that the findings are in good agreement with the measurements on Ag_n.[30] Above all, we can clearly identify icosahedral (Ih) and decahedral (Dh) clusters for large cluster diameters ($d_{Au} > 3$ nm) in numerous cases, two of which are exemplary depicted in Fig. 1. As will be shown later, these structures can be identified as building blocks in conglomerated nanowires.

In order to investigate the aggregation process in the presence of vortices, large He_N ($\bar{N} \approx 1.7 \times 10^{10}$ atoms) are doped with Ag or Au atoms, respectively. In both cases, the doping rate was adjusted so as to obtain either heavy (α = 0.75) or weak (α = 0.2) loading of the droplets. Subsequently, the TEM substrates are exposed to the droplet beam for 5 s. This time is chosen in order to obtain a decent surface coverage on one hand and to ensure an insignificant overlap between nanowires carried by different droplets.

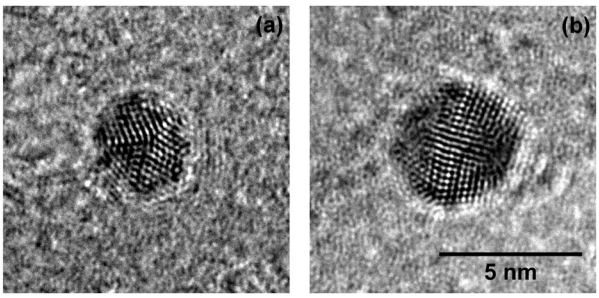

Fig. 1 Decahedral (a) and icosahedral (b) Au_n synthesized in He_N free from vortices ($\bar{N} \approx 7 \times 10^6$ atoms), observed after deposition on a TEM substrate. The morphologies found agree well with those of Ag_n produced under comparable conditions.[30] Scale is the same for both images.

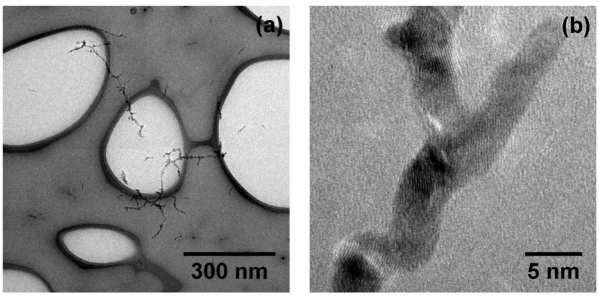

Fig. 2 Ag nanowires synthesized in He_N ($\bar{N} \approx 1.7 \times 10^{10}$), deposited and imaged on a LN_2 cooled (a-c) TEM grid. Continuous branched wires (a) show polycrystalline domains in HRTEM mode (b).

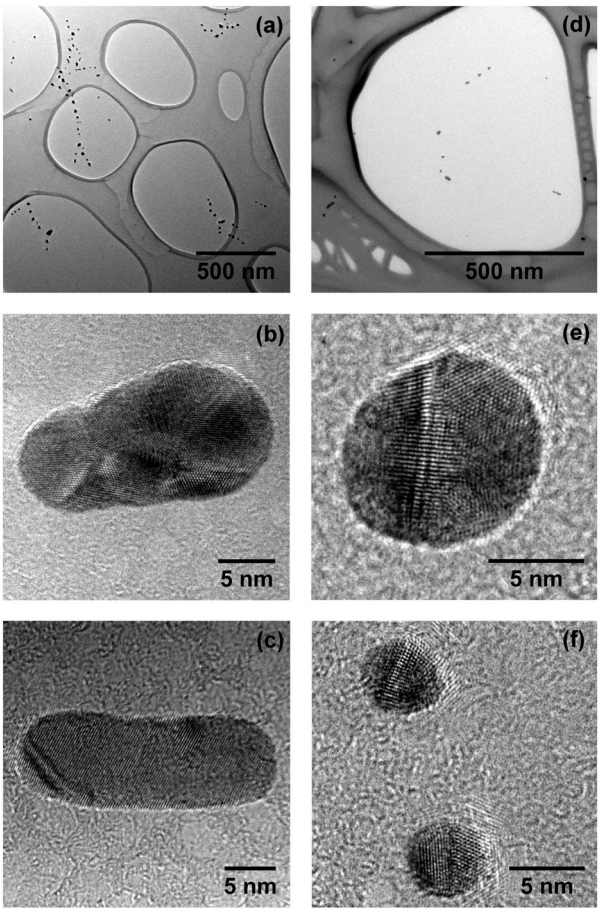

Fig. 3 Chains of Ag segments resulting from the breakup of nanowires as depicted in Fig. 2. Left column: (a) heavy doping of the droplet ($\alpha = 0.75$). HRTEM measurements reveal either polycrystalline morphology (b) or large monocrystalline domains (c). Right column: (d) weak doping ($\alpha = 0.2$). Silver segments resulting from the breakup of small nanowires often exhibit fivefold symmetry, *i.e.* icosahedral ((e), top of (f)) or decahedral (bottom of (f)) morphologies.

Fig. 2(a) shows continuous Ag nanowires with a total length of several hundred nanometers and a mean diameter $\bar{d}_{nw} \approx 5$ nm (as obtained with $\alpha = 0.75$). Cryo-HRTEM measurements on these wires reveal multiple domains of face centered cubic (fcc) morphology (Fig. 2(b)). Blurred parts along the wire are due to thickness oscillations, *i.e.* the structure is visible in the HRTEM measurements only for areas with similar thickness for a chosen defocus. Due to these perturbations in diameter, the wires break up *via* a surface diffusion process already below room temperature, as shown recently.[43] The outcome of this so-called Rayleigh breakup is the occurrence of chains of Ag segments as depicted in Fig. 3(a) and (d), and previously found in other He_N[34,41,44] and He II bulk experiments.[18] HRTEM images reveal that in the case of heavy doping ($\alpha = 0.75$, left column of Fig. 3) these segments can either adopt polycrystalline fcc morphologies (Fig. 3(b)) or exhibit large monocrystalline fcc domains (Fig. 3(c)). No clusters with Ih or Dh morphology were found under these doping conditions.

This is completely different from the findings obtained with Ag and $\alpha = 0.2$ as depicted in the right column of Fig. 3. The existence of large Ihs (Fig. 3(e) and top of Fig. 3(f)) and Dhs (bottom of Fig. 3(f)) is dominating, being followed by particles with large monocrystalline domains. In contrast to the observations made for $\alpha = 0.75$ we find only a very small amount of polycrystalline particles for weak loading of the droplets.

For large Au nanowires ($\alpha = 0.75$) at LN_2 temperature, we find the same branched structures as depicted in Fig. 2(a) for Ag. During the heat-up to room temperature Au nanowires undergo a surface smoothing but do not break into multiple segments (see Fig. 4(a)). The inner morphology (Fig. 4(b)) resembles that of continuous Ag wires, *i.e.* multiple fcc domains can be found. The wires resemble those found in bulk He II experiments in diameter, shape and morphology.[12,13,17,19] Under low doping conditions ($\alpha = 0.2$) we find short but continuous Au wires of slightly smaller diameter (Fig. 4(c)). In numerous cases, these wires contain spherical enclosures of ambiguous morphology, while the rest of the wire consists of multiple fcc domains (Fig. 4(d)).

Further reduction of the amount of doped Au atoms ($\alpha = 0.04$) leads to the observation of segmented Au nanowires (Fig. 5). Assuming conserved volumes, we calculate the mean diameter of the initial wires as $\bar{d}_{nw} \approx 3.0(1)$ nm. The distance between the centers of neighboring segments $\lambda \approx (13 \pm 4)$ nm is in very good agreement with the theoretically derived relationship $2\lambda/d = 8.89$ for the Rayleigh breakup of an ideal cylinder.[71] The HRTEM image in Fig. 5 shows a small

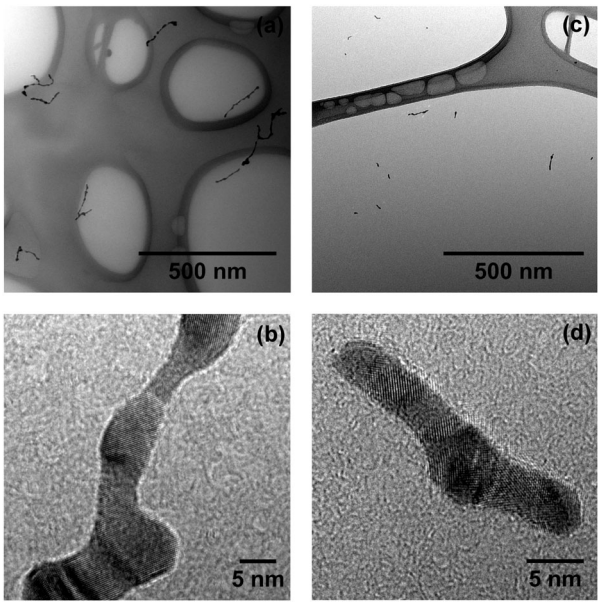

Fig. 4 Au nanowires at room temperature. Left column: heavy doping of the droplet (α = 0.75). Nanowires exhibit a smoothed surface and are continuous over several hundred nanometers (a). Multiple fcc domains are observed along a single wire in HRTEM measurements (b). Right column: weak doping (α = 0.2) leads to short continuous nanowires of about the same diameter (c). HRTEM images (d) reveal spherical enclosures with ambiguous morphology in a wire consisting of several fcc domains.

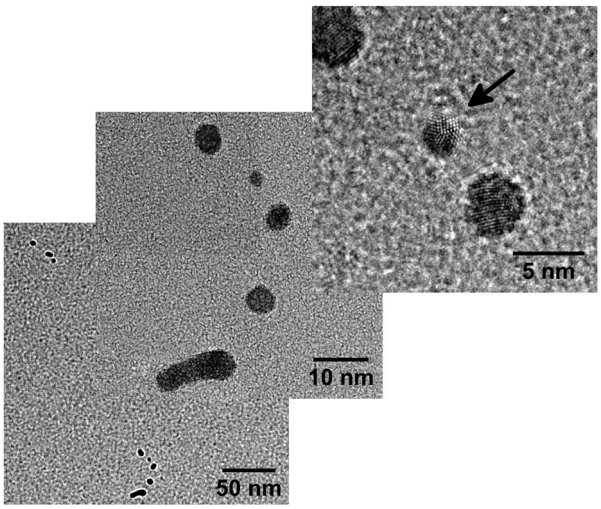

Fig. 5 Segmented Au nanowire resulting from very weak doping (α = 0.04). The arrow marks a small decahedral cluster in the HRTEM image.

decahedral cluster (marked by an arrow) between two clusters of indistinct morphology.

As shown in our previous work,[43] the breakup of Ag nanowires can be explained by the diffusion of wire surface atoms from thinner to thicker parts of the wire due to a gradient of the chemical potential. It is therefore convenient to assume that the observed morphologies are present already inside the initially continuous wires, and that they become clearly visible in the course of the breakup. It has been shown in several theoretical studies that the icosahedral shape is energetically preferred for small metal clusters, while intermediate and large clusters seem to be more stable in Dh and fcc morphologies, respectively (see ref. 72–74 and references therein). Further, it has been determined by MD simulations that the fcc morphology is preferred over the icosahedral morphology for Ag clusters with sizes larger than 1590 atoms ($d_{Ag} \approx 3.7$ nm).[75] The Ihs depicted in Fig. 3(e) and (f) both exhibit diameters larger than 5 nm ($n > 3900$ atoms). Therefore, it can be excluded that they were formed from fcc particles *via* a restructuring process. Such a growth sequence would further strongly contradict MD simulations recently performed by our own group.[47] In simulations of silver clusters we could observe the conversion of Ihs and Dhs into fcc particles during surface deposition due to a recrystallization process, but not a single event of an inverse transformation from fcc into a particle of fivefold symmetry.

4.2 Simulation of the growth process

In order to explain the different morphologies observed we simulate the cluster growth process for different doping rates, *i.e.* different attenuation coefficients α. The maximum simulation time is chosen to equal the mean time it takes for a particle to get trapped by a vortex (t_{trap}). The pickup of atoms and their coagulation into clusters lead to shrinking of the droplets, which influences $\bar{s}$ given in eqn (8). It turns out that t_{trap} is long compared to the timescale of cluster growth, which equals the timescale of the doping process ($\approx$130 μs) determined by the flight time of the He_N through the pickup region. It is therefore convenient to calculate $\bar{s}$ and subsequently t_{trap} using the droplet diameters of the attenuated droplet beam $d_{D,\alpha}$. The results for t_{trap} are summarized in Table 2.

The time evolution of the total number of particles j present in one helium droplet is depicted in Fig. 6 for the attenuations realized in the experiment. It can be seen that in both cases the number of individual particles quickly drops after the pickup of new atoms has ended and that the following agglomeration takes place on a much longer timescale. The reason for this behaviour lies in the slow velocities of large clusters (see eqn (3)) compared to the Landau velocity assumed for freshly spawned metal atoms in the simulation. This finding has also been verified experimentally by the observation of bimetallic core–shell clusters with single or double cores.[49] In order to realize the latter case two clusters have to grow in the droplet in the first of two consecutive pickup regions and have to stay separated until the droplets reach the second pickup cell.

Table 2 Time t_{trap} until particles get trapped by a vortex due to the attractive force given by eqn (6) and (7). $d_{D,\alpha}$ is calculated assuming an initial He_N size of $\bar{N} = 1.7 \times 10^{10}$ atoms. $\bar{s}$ is calculated using eqn (8) and $d_{D,\alpha}$

Element	α	d_D/nm	t_{trap}/ms
Ag	0.75	720	1.4
	0.2	1060	3.0
Au	0.75	720	1.8
	0.2	1060	4.0
	0.04	1130	4.6

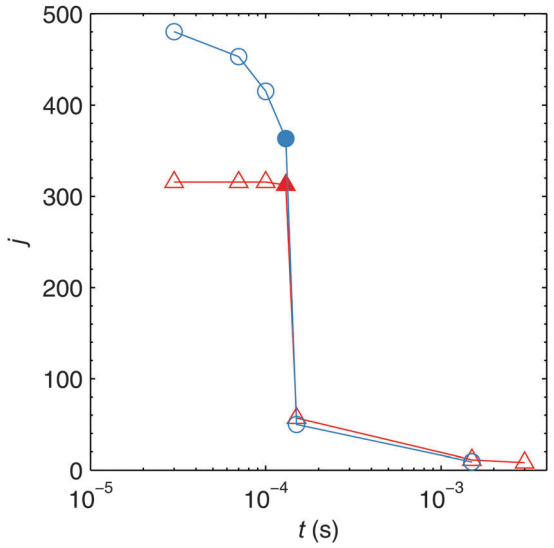

Fig. 6 Time evolution of the number of particles j present in one He_N for α = 0.2 (red triangles) and α = 0.75 (blue circles). The pickup process ends after ≈130 μs, marked by full symbols. Lines are drawn to guide the eye.

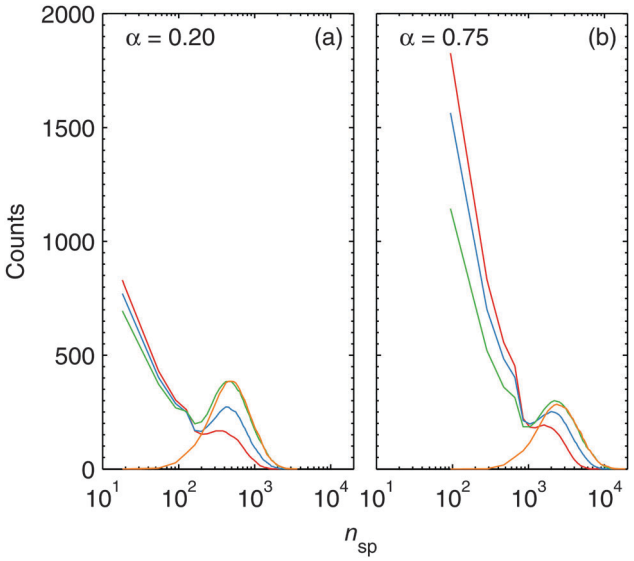

Fig. 7 Number of atoms n_{sp} building up the spherical clusters contained in a single He_N for α = 0.2 (a) and α = 0.75 (b). Lines are envelopes of histograms taken at different times of the aggregation process: 30 μs (red), 70 μs (blue), 130 μs (green), 150 μs (orange).

The corresponding He_N flight time can be estimated as ≈1 ms in our apparatus.[50]

Fig. 6 also reveals a decrease of j during the pickup process for larger attenuations, while j seems to stay nearly constant for α = 0.2. This behaviour can be explained by the shrinking of He_N which is much more prominent for α = 0.75 as can be seen from Table 2. The He_N flight time between the pickup cell and the TEM substrate is ≈6 ms. Comparing this to the timescale of cluster growth and to t_{trap}, it is evident that most clusters have to grow outside the vortex in a multicenter aggregation process, and that nearly all clusters will be captured by the vortex before substrate deposition.

The monitoring of the number of particles contained in spherical clusters n_{sp} can give us a further important insight into the agglomeration process. Fig. 7 depicts the absolute occurrence of a certain value of n_{sp} for all spherical particles contained in a single He_N. The lines shown correspond to the smoothed envelopes of histograms. Every histogram is calculated from several simulation runs for every depicted time of the aggregation process. Snapshots are taken during the pickup process at 30, 70, 130 (end of the pickup) and at 150 μs. As explained in the computational details, spherical clusters which do not melt during agglomeration are treated as elongated particles, built from the initially spherical collision partners. n_{sp} includes all spherical clusters, regardless of whether they are present as building blocks of elongated structures or as individual spheres. From this, it follows that Fig. 7 directly reflects the sizes of the last complete melting of the clusters. A merging event which does not lead to molten clusters does affect j, but not the depicted histograms of n_{sp}.

The large amount of small clusters present in the droplets during the pickup process is efficiently reduced after the addition of new atoms has ended, which is in good agreement with the behaviour depicted in Fig. 6. In fact, the final distribution of spherical building blocks is reached after 150 μs. This means that melting processes are practically limited to the pickup time, and that 20 μs after the end of pickup melting is negligible. After 150 μs, the spherical clusters still coagulate to form the final nanoparticles. This process takes the time which we calculated as t_{trap} earlier.

The most striking feature in Fig. 7 is that the positions of the histogram maxima are determined by the attenuation, *i.e.* the doping rate. A high doping rate in the case of α = 0.75 leads to a stronger heating of the clusters as more atoms impinge within a given time while the cooling rate r_c is the same as for weaker doping. The effect is further enhanced by the pronounced shrinking of the droplet under heavy doping conditions, and leads to a slight shift of the histogram maxima towards higher values of n_{sp} in Fig. 7. We can extract from the histograms $\bar{n}_{sp} \approx 600$ ($\bar{d}_{Ag} \approx 2.7$ nm) for α = 0.2 and $\bar{n}_{sp} \approx 3000$ ($\bar{d}_{Ag} \approx 4.6$ nm) for α = 0.75, which are also in good agreement with the diameters observed for deposited nanowires in the cryo-TEM images. As explained above, the fcc structure is energetically preferred over the Ih morphology for cluster sizes larger than 1590 atoms ($d_{Ag} \approx 3.7$ nm).[75] Since the clusters solidify from a molten state, it is justified to assume that the formation of Ihs is much more probable at α = 0.2 than it is for α = 0.75. This explains the exclusive findings of particles of fivefold symmetry under weak doping conditions in the experiment.

5 Conclusions

Experimentally observed morphologies of He_N-grown Au and Ag nanowires depend on the rate of doping with metal atoms during the pickup process. In the first step of the growth process, multiple clusters are formed within a droplet in a

multicenter aggregation process. At low doping rates, a large portion of these clusters exhibits fivefold symmetry, while at high rates the presence of the fcc structure is dominating. In the second step of the growth process these clusters are captured by vortices and coagulate into nanowires. According to our simulations, their coagulation does not result in a complete melting of the single clusters. This is related to the large cluster sizes and the relatively low collision rates at this stage of the nanowire growth. Therefore, the morphologies of the initial building blocks, *i.e.* the coagulating clusters, are preserved within the nanowires.

We believe that our experimental findings and the computational model presented will be of use in future attempts of gaining better control over the synthesis and the design of nanostructures within He_N. It would also be desirable to determine the morphologies of clusters enclosed in the He_N before substrate deposition, *e.g.* by X-ray scattering, a technique which has been exploited recently to investigate the morphologies of large free Ag nanoparticles.[76]

Acknowledgements

The authors thank Dr Markus Koch and Dr Florian Lackner for fruitful discussions and Manuel Paller for creating 3D graphics. This research has been supported by the Austrian Science Fund (FWF) under Grant FWF-E-P22962, by the European Commission and the Styrian Government within the ERDF program as well as by the European Union within the 7th Framework Programme (FP7/2007-2013) under Grant Agreement No. 312483 (ESTEEM2). The authors gratefully acknowledge support from NAWI Graz.

References

1 L. Onsager, *Proc. Int. Conf. Theor. Phys.*, Science Council of Japan, Tokyo, 1953, pp. 877–880.
2 R. P. Feynman, in *Progress in Low Temperature Physics*, ed. C. J. Gorter, North-Holland, Amsterdam, 1955, pp. 17–53.
3 G. A. Williams and R. E. Packard, *Phys. Rev. Lett.*, 1974, **33**, 280–283.
4 E. J. Yarmchuk, M. J. V. Gordon and R. E. Packard, *Phys. Rev. Lett.*, 1979, **43**, 214–217.
5 G. P. Bewley, D. P. Lathrop and K. R. Sreenivasan, *Nature*, 2006, **441**, 588.
6 R. J. Donelly, *Quantized Vortices in Helium II*, Cambridge University Press, Cambridge, 1991.
7 G. P. Bewley, M. S. Paoletti, K. R. Sreenivasan and D. P. Lathrop, *Proc. Natl. Acad. Sci. U. S. A.*, 2008, **105**, 13707–13710.
8 M. S. Paoletti, M. E. Fisher, K. R. Sreenivasan and D. P. Lathrop, *Phys. Rev. Lett.*, 2008, **101**, 154501.
9 M. S. Paoletti, M. E. Fisher and D. P. Lathrop, *Phys. D*, 2010, **239**, 1367–1377.
10 E. B. Gordon and Y. Okuda, *J. Low Temp. Phys.*, 2009, **35**, 209–213.
11 E. B. Gordon, A. V. Karabulin, V. I. Matyushenko, V. D. Sizov and I. I. Khodos, *J. Low Temp. Phys.*, 2010, **36**, 590–595.
12 P. Moroshkin, V. Lebedev, B. Grobety, C. Neururer, E. B. Gordon and A. Weis, *EPL*, 2010, **90**, 34002.
13 V. Lebedev, P. Moroshkin, B. Grobety, E. Gordon and A. Weis, *J. Low Temp. Phys.*, 2011, **165**, 166–176.
14 E. B. Gordon, A. V. Karabulin, V. I. Matyushenko, V. D. Sizov and I. I. Khodos, *J. Exp. Theor. Phys.*, 2011, **112**, 1061–1070.
15 E. B. Gordon, A. V. Karabulin, V. I. Matyushenko, V. D. Sizov and I. I. Khodos, *Appl. Phys. Lett.*, 2012, **101**, 052605.
16 E. Gordon, A. Karabulin, V. Matyushenko, V. Sizov and I. Khodos, *Chem. Phys. Lett.*, 2012, **519–520**, 64–68.
17 E. B. Gordon, A. V. Karabulin, A. A. Morozov, V. I. Matyushenko, V. D. Sizov and I. I. Khodos, *J. Phys. Chem. Lett.*, 2014, **5**, 1072–1076.
18 E. Gordon, A. Karabulin, V. Matyushenko, V. Sizov and I. Khodos, *Phys. Chem. Chem. Phys.*, 2014, **16**, 25229–25233.
19 E. B. Gordon, A. V. Karabulin, V. I. Matyushenko and I. I. Khodos, *J. Phys. Chem. A*, 2015, **119**, 2490–2501.
20 E. B. Gordon, A. V. Karabulin, V. I. Matyushenko, V. D. Sizov and I. I. Khodos, *Laser Phys. Lett.*, 2015, **12**, 096002.
21 J. P. Toennies and A. F. Vilesov, *Angew. Chem., Int. Ed.*, 2004, **43**, 2622–2648.
22 J. Tiggesbäumker and F. Stienkemeier, *Phys. Chem. Chem. Phys.*, 2007, **9**, 4748–4770.
23 C. Callegari and W. E. Ernst, in *Handbook of High Resolution Spectroscopy*, ed. F. Merkt and M. Quack, John Wiley & Sons, Chichester, 2011, vol. 3, pp. 1551–1594.
24 M. Mudrich and F. Stienkemeier, *Int. Rev. Phys. Chem.*, 2014, **33**, 301–339.
25 M. Theisen, F. Lackner and W. E. Ernst, *J. Phys. Chem. A*, 2011, **115**, 7005–7009.
26 M. Ratschek, M. Koch and W. E. Ernst, *J. Chem. Phys.*, 2012, **136**, 104201.
27 V. Mozhayskiy, M. N. Slipchenko, V. K. Adamchuk and A. F. Vilesov, *J. Chem. Phys.*, 2007, **127**, 094701.
28 E. Loginov, L. F. Gomez and A. F. Vilesov, *J. Phys. Chem. A*, 2011, **115**, 7199–7204.
29 A. Boatwright, C. Feng, D. Spence, E. Latimer, C. Binns, A. M. Ellis and S. Yang, *Faraday Discuss.*, 2013, **162**, 113–124.
30 A. Volk, P. Thaler, M. Koch, E. Fisslthaler, W. Grogger and W. E. Ernst, *J. Chem. Phys.*, 2013, **138**, 214312.
31 S. Yang, A. M. Ellis, D. Spence, C. Feng, A. Boatwright, E. Latimer and C. Binns, *Nanoscale*, 2013, **5**, 11545–11553.
32 S. B. Emery, K. B. Rider, B. K. Little, A. M. Schrand and C. M. Lindsay, *J. Chem. Phys.*, 2013, **139**, 054307.
33 S. B. Emery, K. B. Rider and C. M. Lindsay, *Propellants, Explos., Pyrotech.*, 2014, **39**, 161–165.
34 L. F. Gomez, E. Loginov and A. F. Vilesov, *Phys. Rev. Lett.*, 2012, **108**, 155302.
35 F. Dalfovo, R. Mayol, M. Pi and M. Barranco, *Phys. Rev. Lett.*, 2000, **85**, 1028–1031.
36 K. K. Lehmann and R. Schmied, *Phys. Rev. B: Condens. Matter Mater. Phys.*, 2003, **68**, 224520.
37 F. Ancilotto, M. Barranco and M. Pi, *Phys. Rev. Lett.*, 2003, **91**, 105302.
38 E. Sola, J. Casulleras and J. Boronat, *Phys. Rev. B: Condens. Matter Mater. Phys.*, 2007, **76**, 052507.

39 L. F. Gomez, K. R. Ferguson, J. P. Cryan, C. Bacellar, R. M. P. Tanyag, C. Jones, S. Schorb, D. Anielski, A. Belkacem, C. Bernando, R. Boll, J. Bozek, S. Carron, G. Chen, T. Delmas, L. Englert, S. W. Epp, B. Erk, L. Foucar, R. Hartmann, A. Hexemer, M. Huth, J. Kwok, S. R. Leone, J. H. S. Ma, F. R. N. C. Maia, E. Malmerberg, S. Marchesini, D. M. Neumark, B. Poon, J. Prell, D. Rolles, B. Rudek, A. Rudenko, M. Seifrid, K. R. Siefermann, F. P. Sturm, M. Swiggers, J. Ullrich, F. Weise, P. Zwart, C. Bostedt, O. Gessner and A. F. Vilesov, *Science*, 2014, **345**, 906–909.
40 F. Ancilotto, M. Pi and M. Barranco, *Phys. Rev. B: Condens. Matter Mater. Phys.*, 2015, **91**, 100503.
41 E. Latimer, D. Spence, C. Feng, A. Boatwright, A. M. Ellis and S. Yang, *Nano Lett.*, 2014, **14**, 2902–2906.
42 P. Thaler, A. Volk, F. Lackner, J. Steurer, D. Knez, W. Grogger, F. Hofer and W. E. Ernst, *Phys. Rev. B: Condens. Matter Mater. Phys.*, 2014, **90**, 155442.
43 A. Volk, D. Knez, P. Thaler, A. W. Hauser, W. Grogger, F. Hofer and W. E. Ernst, *Phys. Chem. Chem. Phys.*, 2015, **17**, 24570–24575.
44 D. Spence, E. Latimer, C. Feng, A. Boatwright, A. M. Ellis and S. Yang, *Phys. Chem. Chem. Phys.*, 2014, **16**, 6903–6906.
45 M. P. de Lara-Castells, N. F. Aguirre, H. Stoll, A. O. Mitrushchenkov, D. Mateo and M. Pi, *J. Chem. Phys.*, 2015, **142**, 131101.
46 V. N. Popok, I. Barke, E. E. B. Campbell and K.-H. Meiwes-Broer, *Surf. Sci. Rep.*, 2011, **66**, 347–377.
47 P. Thaler, A. Volk, M. Ratschek, M. Koch and W. E. Ernst, *J. Chem. Phys.*, 2014, **140**, 044326.
48 A. W. Hauser, A. Volk, P. Thaler and W. E. Ernst, *Phys. Chem. Chem. Phys.*, 2015, **17**, 10805–10812.
49 G. Haberfehlner, P. Thaler, D. Knez, A. Volk, F. Hofer, W. E. Ernst and G. Kothleitner, *Nat. Commun.*, 2015, **6**, 8779.
50 P. Thaler, A. Volk, D. Knez, F. Lackner, G. Haberfehlner, J. Steurer, M. Schnedlitz and W. E. Ernst, *J. Chem. Phys.*, 2015, **143**, 134201.
51 L. F. Gomez, E. Loginov, R. Sliter and A. F. Vilesov, *J. Chem. Phys.*, 2011, **135**, 154201.
52 H. Buchenau, E. L. Knuth, J. Northby, J. P. Toennies and C. Winkler, *J. Chem. Phys.*, 1990, **92**, 6875–6889.
53 D. M. Brink and S. Stringari, *Z. Phys. D*, 1990, **15**, 257–263.
54 A. Leal, D. Mateo, A. Hernando, M. Pi, M. Barranco, A. Ponti, F. Cargnoni and M. Drabbels, *Phys. Rev. B: Condens. Matter Mater. Phys.*, 2014, **90**, 224518.
55 D. Mateo, A. Leal, A. Hernando, M. Barranco, M. Pi, F. Cargnoni, M. Mella, X. Zhang and M. Drabbels, *J. Chem. Phys.*, 2014, **140**, 131101.
56 A. Leal, D. Mateo, A. Hernando, M. Pi and M. Barranco, *Phys. Chem. Chem. Phys.*, 2014, **16**, 23206–23213.
57 C. Kittel, *Introduction to Solid State Physics*, John Wiley & Sons, Hoboken, 2005.
58 M. D. Morse, *Chem. Rev.*, 1986, **86**, 1049–1109.
59 M. Hartmann, R. E. Miller, J. P. Toennies and A. Vilesov, *Phys. Rev. Lett.*, 1995, **75**, 1566–1569.
60 M. Hartmann, N. Pörtner, B. Sartakov, J. P. Toennies and A. F. Vilesov, *J. Chem. Phys.*, 1999, **110**, 5109–5123.
61 N. B. Brauer, S. Smolarek, E. Loginov, D. Mateo, A. Hernando, M. Pi, M. Barranco, W. J. Buma and M. Drabbels, *Phys. Rev. Lett.*, 2013, **111**, 153002.
62 H. Müller, H.-G. Fritsche and L. Skala, in *Clusters of Atoms and Molecules I*, ed. H. Haberland, Springer-Verlag, Berlin Heidelberg, 1995.
63 C. M. Lindsay and R. E. Miller, *J. Chem. Phys.*, 2005, **122**, 104306.
64 I. Scheele, A. Conjusteau, C. Callegari, R. Schmied, K. K. Lehmann and G. Scoles, *J. Chem. Phys.*, 2005, **122**, 104307.
65 E. Popov, M. Mammetkuliyev and J. Eloranta, *J. Chem. Phys.*, 2013, **138**, 204307.
66 D. P. Meichle and D. P. Lathrop, *Rev. Sci. Instrum.*, 2014, **85**, 073705.
67 T. V. Chagovets and S. W. Van Sciver, *Phys. Fluids*, 2011, **23**, 107102.
68 Y. A. Sergeev and C. F. Barenghi, *J. Low Temp. Phys.*, 2009, **157**, 429–475.
69 J. Schindelin, I. Arganda-Carreras, E. Frise, V. Kaynig, M. Longair, T. Pietzsch, S. Preibisch, C. Rueden, S. Saalfeld, B. Schmid, J.-Y. Tinevez, D. J. White, V. Hartenstein, K. Eliceiri, P. Tomancak and A. Cardona, *Nat. Methods*, 2012, **9**, 676–682.
70 K. Koga and K. Sugawara, *Surf. Sci.*, 2003, **529**, 23–35.
71 F. A. Nichols and W. W. Mullins, *Trans. Metall. Soc. AIME*, 1965, **233**, 1840–1848.
72 F. Baletto and R. Ferrando, *Rev. Mod. Phys.*, 2005, **77**, 371–423.
73 F. Baletto, R. Ferrando, A. Fortunelli, F. Montalenti and C. Mottet, *J. Chem. Phys.*, 2002, **116**, 3856–3863.
74 F. Baletto, C. Mottet and R. Ferrando, *Chem. Phys. Lett.*, 2002, **354**, 82–87.
75 C. Amano, H. Niina and Y. Mikami, *THEOCHEM*, 2009, **904**, 64–68.
76 I. Barke, H. Hartmann, D. Rupp, L. Flückiger, M. Sauppe, M. Adolph, S. Schorb, C. Bostedt, R. Treusch, C. Peltz, S. Bartling, T. Fennel, K.-H. Meiwes-Broer and T. Müller, *Nat. Commun.*, 2015, **6**, 6187.